*minerals*

MDPI

*Article*

# Petrogenesis and Geodynamic Implications of the North Kudi Granitoids in the West Kunlun Orogen, NW China

**Kai Wu [1,*], Meijun Gong [1], Xiaoyan Jiang [2], Mingxing Ling [3] and Honglin Yuan [1]**

[1] State Key Laboratory of Continental Dynamics, Department of Geology, Northwest University, Xi'an 710069, China; hlyuan@nwu.edu.cn (H.Y.)
[2] State Key Laboratory of Ore Deposit Geochemistry, Institute of Geochemistry, Chinese Academy of Sciences, Guiyang 550081, China
[3] State Key Laboratory of Nuclear Resources and Environment, East China University of Technology, Nanchang 330013, China
* Correspondence: wukai@nwu.edu.cn

**Abstract:** The petrogenesis of aluminous A-type granites is a contentious subject. Here, we focused on the North Kudi pluton in the Western Kunlun orogen to investigate the origin and magmatic processes responsible for generating A-type granites. Samples from the North Kudi pluton are metaluminous to weakly peraluminous. K-feldspar granite samples are characterized by high alkali and Cl contents, high HFSE concentrations and FeO/MgO, low F content, negative Ba, Sr, P, Eu, and Ti anomalies, and high magma temperature (>903 °C), showing affinity to aluminous A-type granites. However, their 10,000 × Ga/Al ratios (1.86–3.18) are relatively lower than typical A-type granites. Quartz-monzonite displays similar Sr–Nd isotopic compositions and Ga/Al ratios with the K-feldspar granite but less pronounced negative Sr, P, and Ti anomalies and no discernable negative Ba and Eu anomalies. Fractional crystallization of alkali-rich, Cl-rich, and F-poor magmas can generate some typical geochemical characteristics of A-type granites (e.g., negative Ba, Sr, P, and Eu anomalies) but has little influence on Ga/Al ratios. The enriched Sr–Nd isotopic compositions, high Cl and alkali contents, arc-like geochemical features, and the involvement of slab-derived components, as indicated by high zircon $Ce^{4+}/Ce^{3+}$ (up to 503), suggest that the North Kudi pluton was possibly derived from partial melting of the metasomatized lithospheric mantle in the time of asthenosphere upwelling during the post-collisional stage. The emplacement of the North Kudi pluton thus indicates the onset of the post-orogenic stage in the Western Kunlun orogen.

**Keywords:** A-type granite; Western Kunlun; Proto-Tethys



**Citation:** Wu, K.; Gong, M.; Jiang, X.; Ling, M.; Yuan, H. Petrogenesis and Geodynamic Implications of the North Kudi Granitoids in the West Kunlun Orogen, NW China. *Minerals* **2023**, *13*, 941. https://doi.org/10.3390/min13070941

Academic Editor: Jaroslav Dostal

Received: 16 May 2023
Revised: 10 July 2023
Accepted: 11 July 2023
Published: 14 July 2023



## 1. Introduction

A-type granites are defined initially as anorogenic granites that occur in a rift zone or stable continental block [1–4]. They can be distinguished from typical calc-alkaline I-type granites by their "mildly alkaline" (alkalic to alkali-calcic) with high F, rare earth element (REE) (except for Eu), and high field strength element (HFSE) concentrations, high FeO/MgO and Ga/Al ratios, but low Ca, Ba and Sr abundances [1,4–11]. Subsequent studies showed that the original definition of "A-type granite" cannot adequately describe the distinct group [6,12], which leads to further divisions. For example, A-type granites have been divided into $A_1$- and $A_2$- subgroups, where the former subgroup share similar geochemical characteristics with oceanic-island basalts, whereas the latter commonly occur in post-collisional settings with arc-like geochemical compositions [6,13,14]. The term "A-type granite" has also been applied to some calc-alkalic granitoids with Fe-rich minerals, high $Fe^{total}/(Fe^{total} + Mg)$ ratio, and high REE, HFSE, Ga, and Zn concentrations in southwestern Australia, which are metaluminous to weakly peraluminous rather than peralkaline [5]. Subsequently, this type of metaluminous to weakly peraluminous A-type granites in the Lachlan Fold Belt was defined as "aluminous A-type granites" [12]. In

addition, A-type granites are also divided into reduced and oxidized subgroups according to the water content and redox state during the formation processes [3,15–17]. The oxidized A-type granitic magmas can contain significant amounts of $H_2O$ ($\geq$4 wt.%), while the reduced subtype was suggested to be derived from an $H_2O$-poor magma source [16,17]. In summary, although A-type granites can be divided into different subtypes according to different classification schemes, there is a consensus that A-type granites were formed under different extensional settings through various mechanisms.

Possible mechanisms responsible for the generation of peralkaline A-type granites include fractional crystallization of mantle-derived alkaline magmas and mixing between mantle-derived and crustal melts [6,18–20]. Aluminous A-type granites generally occur at the final stage of post-collisional magmatism and are spatially and temporally associated with post-collisional I-type granites [21–23]. Since aluminous A-type granites usually contain high $SiO_2$ but extremely low MgO and CaO contents and low Cr, Co, and Ni concentrations, some studies suggested that aluminous A-type granites were formed by partial melting of a felsic infracrustal source [12,22,24]. However, the genesis of the aluminous A-type has also been attributed to the partial melting of a slightly metasomatized mantle with subduction contributions [21,25]. The Kudi pluton in the Western Kunlun orogen comprises quartz-monzonite and K-feldspar granite [26,27]. In previous studies, the K-feldspar granite was classified as aluminous A-type granites associated with partial melting of a crustal source consisting of the Precambrian metasedimentary and metaigneous rocks in the Western Kunlun orogen, which marks the onset of the post-orogenic stage [26,27]. However, the K-feldspar granite samples in the literature also demonstrate some geochemical features that are different from typical A-type granites (e.g., relatively lower 10,000 $\times$ Ga/Al). In addition, little effort has been made to investigate the genetic relationship between these quartz-monzonites and K-feldspars granite. The temporally and spatially coexisting intermediate granitoids and metaluminous to peraluminous granites with A-type affinities provide an excellent opportunity to investigate the possibility of fractional crystallization of alkaline magmas to generate the geochemical features of typical aluminous A-type granites. In this paper, we presented new and more detailed zircon U–Pb age and Hf isotopic data, whole-rock major and trace element, and Sr–Nd isotopic compositions of quartz-monzonite and K-feldspar granite in the North Kudi pluton, which can not only provide new information on the origin and genesis of the North Kudi pluton but also provide new insights into the tectonic evolution of the Western Kunlun orogen.

## 2. Geological Setting and Sample Descriptions

The Western Kunlun orogen in central Asia links the Pamir syntaxis to the west and the East Kunlun orogen to the east and is considered as the northwestern margin of the Tibetan Plateau [28–30]. It is separated by the Meso-Cenozoic Altyn fault [31,32] and contains two important sutures, the Kudi-Qimanyute suture in the north and the Mazha-Kangxiwa suture in the south [27,29]. The Kegang fault separates the North Kunlun Terrane (NKT) and the Tarim Craton (Figure 1). Previous studies suggested that they have a similar Precambrian metamorphic basement, which is overlain by the Devonian molasse and Carboniferous-Permian shallow marine carbonates [28,33,34].

The South Kunlun Terrane (SKT) is separated from the NKT by the Kudi-Qimanyute suture. The Kudi-Qimanyute suture contains a series of ophiolite slices, including the Kudi ophiolite and the Qimanyute ophiolite [27]. The Kudi ophiolite suite comprises ultramafic rocks, volcanic and volcanoclastic rocks, and forearc sediments, representing an obducted ophiolite slice with ages of 490–525 Ma [27,30,32,35]. The Qimanyute ophiolite comprises peridotite, gabbros, diabase sheet, and basaltic pillow lavas. The layered gabbros in the Qimanyute ophiolite were formed at ~526 Ma and were intruded by Late Ordovician granitic rocks [36]. The outcropped Precambrian strata in the SKT contain the Pushou Group and the Sangzhutage Group in the north and the Saitula Group in the South, separated by the Pushou-Menggubao ophiolitic mélange [37]. The Pushou Group comprises metasedimentary rocks in high amphibolite facies, and the Sangzhutage Group consists of

green schist-facies metasedimentary rocks [37–39]. A granodioritic intrusion intruded into the Sangzhutage Group at ~505 Ma [40]. The Saitula Group comprises gneiss and schist with minor intercalated amphibolite [39].

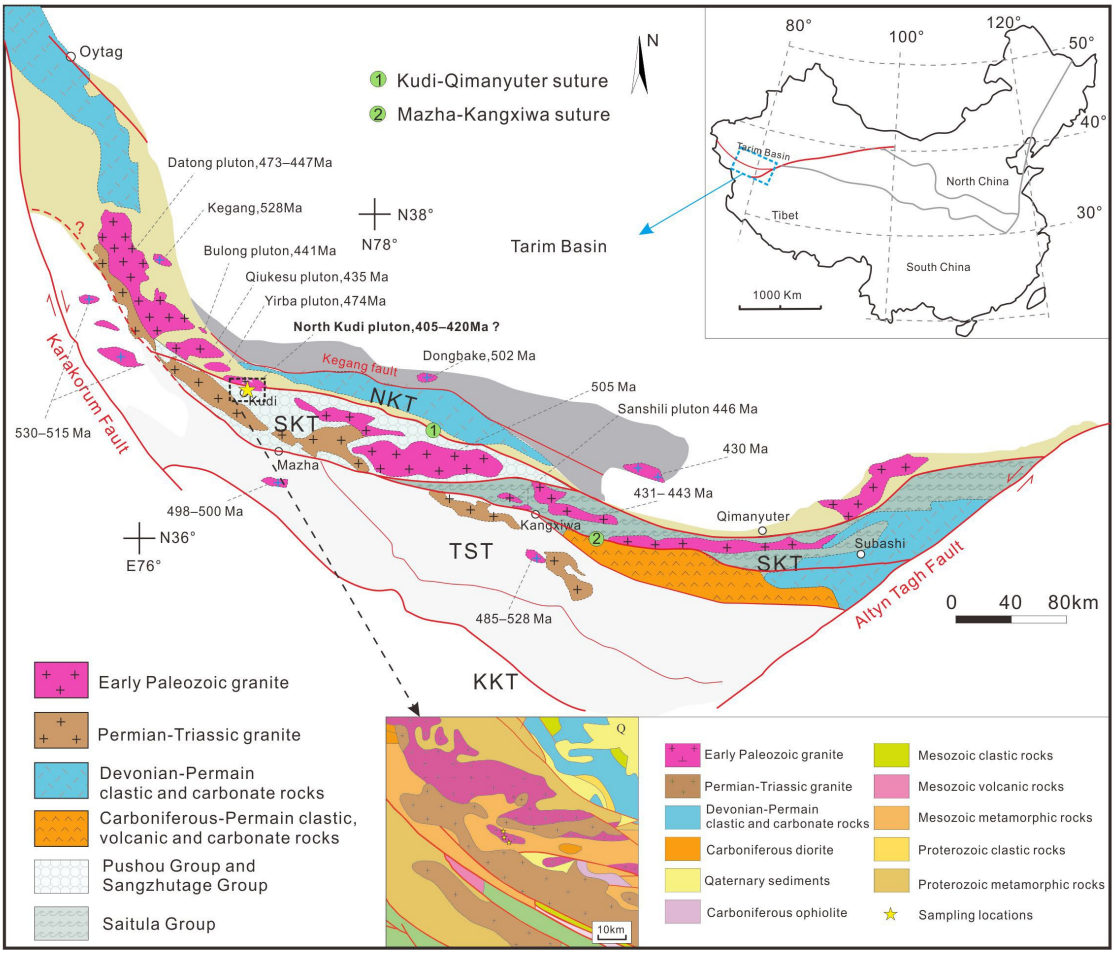


**Figure 1.** Simplified geological map of the Western Kunlun orogen (modified from [40]) illustrating the sampling location.

The Tianshuihai Terrane (TSHT) and the SKT are separated by the Mazha-Kangxiwa suture, which is mainly composed of arc complexes and a suit of volcanic-sedimentary rocks. The hornblende quartz diorite from the arc complexes in the Mazha-Kangxiwa suture is emplaced at ~338 Ma [41]. There are also some high-pressure (HP) granulite blocks in this suture, which have a protolith age of ~456 Ma and were subjected to an amphibolite-facies metamorphic event at ~177 Ma [42,43]. The TSHT comprises meta-greywackes and limestone, which were considered as a huge accretionary wedge associated with a Late Paleozoic-Early Mesozoic orogenic process in some previous studies [30,40,44]. However, some Paleoproterozoic metavolcanic rocks were discovered recently, which indicates the existence of the Precambrian basement beneath the TSHT [45].

The granitic magma setting in the Western Kunlun orogen provides essential clues for the tectonic evolution of the Proto- and Paleo-Tethys Oceans. Early studies distinguished two granitoid belts parallel to the suture zones in the Western Kunlun orogen, with the Early Paleozoic belt in the north and the Early Mesozoic one in the south [46]. The former contains the Datong complex and the Quekesu, Yirba, North Kudi, and some small intrusions (Figure 1). Recent studies also reported some Early Paleozoic granitoids in the Tianshuihai terrane, such as the Kelule, Nanpingxueshan, Ayilixi, and Warengzilafu plutons [47–49].

In this contribution, we focus on the Early Paleozoic North Kudi pluton, which was classified as an $A_1$-type intrusion in previous studies [26,27,44]. The North Kudi pluton is located 7 km north of the Kudi village. The North Kudi pluton intruded into the Sangzhutage Group in the South Kunlun terrane, which consists of quartz-monzonite and K-feldspar granite (Figure 1). Quartz-monzonite samples are mainly distributed in the northern part of the pluton, whereas the K-feldspar granite primarily occurs in the southern part of the pluton. However, the petrogenesis of these quartz-monzogranites has not been investigated in previous studies. Quartz-monzonite and K-feldspar granite samples from the North Kudi pluton display a massive structure and medium-grained texture. The quartz monzogranites consist of plagioclase (30%–40%), K-feldspar (30%–45%), quartz (15%–20%), and biotite (7%–10%) (estimated under the polarizing microscope) (Figure 2). Accessory minerals include sphene, apatite, zircon, monazite, and magnetite. K-feldspar granites are composed of K-feldspar (60%–70%), plagioclase (8%–15%), quartz (20%–25%), and biotite (3%–5%) with minor magnetite, zircon, apatite, and sphene.

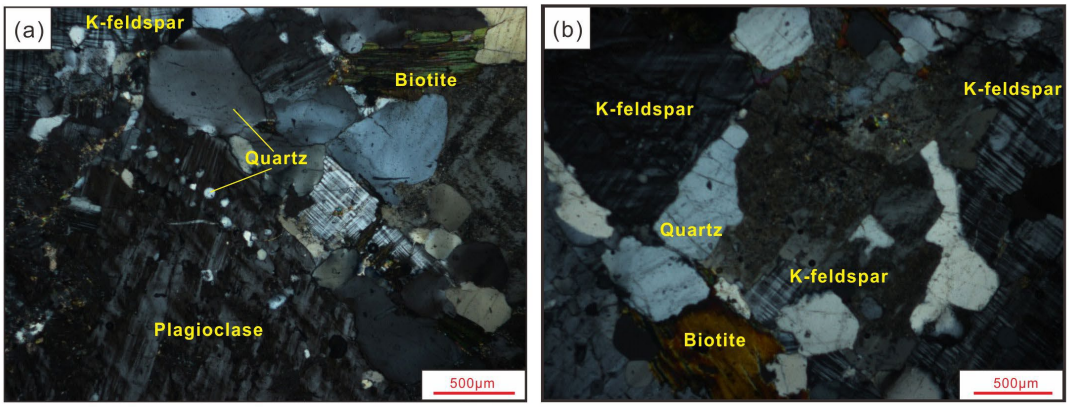


**Figure 2.** Photomicrographs of representative quartz-monzonite (**a**) and K-feldspar granite (**b**) samples from the North Kudi pluton. Both quartz-monzonite (**a**) and K-feldspar granite display medium-grained texture.

## 3. Analytical Methods

### *3.1. Zircon U–Pb Dating and Hf Isotopes*

Zircon U–Pb dating and Hf isotope analysis were all conducted at the State Key Laboratory of Isotope Geochemistry, Guangzhou Institute of Geochemistry, Chinese Academy of Sciences (SKLIG-GIG-CAS). An Agilent 7900 ICP-MS (Agilent Technologies, Inc., Santa Clara, CA, USA) is equipped with a Resonetics RESOlution S155 laser-ablation system (LA) to perform zircon U–Pb dating and trace element analyses. Helium was used as a carrier gas [50]. The repletion rate was set to be 8 Hz, laser energy to be 85 mJ, ablating time to be 45 s, and spot size to be 31 μm. International standards TEMORA and NIST SRM 610 were used as the external calibration standard for zircon U–Pb ages and trace element contents. $^{91}$Zr was chosen as the internal standard for zircon trace element analysis with uncertainties of 5% [25]. The standard reference zircon, Qinghu, was also analyzed during our experiments to monitor the dating results, and the mean $^{206}Pb/^{238}U$ age of the analyzed Qinghu zircon grains is 158 ± 3 Ma, which is within the recommended value [51]. Since previous studies have already provided zircon SHRIMP U–Pb age data for the K-feldspar granite [26,27], our study only focused on zircon grains separated from a quartz monazite sample. Zircon age and trace element data processing were performed with ICPMSDataCal 7.2 [52]. In situ zircon Lu–Hf isotopic compositions were analyzed on the same zircon domain with a spot size of 44 μm in diameter, which has been previously ablated during LA-ICP-MS zircon dating. The ablation time is 60 s, with an energy density of 20 J/cm$^2$ and a repletion rate of 8 Hz [53]. The $^{176}$Lu decay constant is $1.867 \times 10^{-11}$ yr$^{-1}$ in our calculation of the initial $^{176}Lu/^{177}Hf$. The εHf(t) was calculated relative to the chondritic reservoir with $^{176}Lu/^{177}Hf = 0.0336$ and $^{176}Hf/^{177}Hf = 0.282725$ [54].

### *3.2. Whole-Rock Major and Trace Elements*

Major and trace elements measurements were also analyzed at SKLIG-GIG-CAS. Major element concentrations of our samples were measured via X-ray fluorescence spectrometry (XRF). Sample powders (0.51–0.53 g) were firstly fluxed with $Li_2B_4O_7$ to make homogeneous glass disks at 1050–1100 °C for XRF analysis. The analytical errors for major elements are better than 1%. The trace element analyses were carried out by ablating fluxed glass disks (with the sample to $Li_2B_4O_7$ ratio of 1:3) via LA-ICPMS. An Agilent 7500 ICP-MS is coupled with a Resonetics RESOlution M-50 ArF-Excimer laser-ablation system for trace element measurements. The repetition rate is 6 Hz with a laser energy of 80 mJ and a spot size of 69 μm. NIST 610 was used as an external standard, and $^{29}Si$ as the internal standard for trace element analysis [25]. Data processing is carried out with ICPMSDataCal 7.2 [52]. Fluorite and chlorite content measurement were conducted at the ALS Mineral Laboratory in Guangzhou, China. Sample powder was digested with KOH in a nickel crucible and dissolved in $HNO_3$ solutions. The solution was analyzed via Metrohm IC 930 ion chromatography to obtain the fluorite and chlorite contents.

### *3.3. Whole-Rock Sr–Nd Isotope*

Whole-rock Sr–Nd isotope compositions were analyzed via a Multi-collector Inductively Coupled Plasma Mass Spectrometry (MC-ICP-MS) at the University of Science and Technology of China after chemical separation and purification in SKLIG-GIG-CAS after careful column chemistry at SKLIG-GIG-CAS. Details about chemical separation and purification procedures were presented in the literature [55]. The international standard, BHVO-2, was used as the standard for isotopic ratio analysis. The mean Sr–Nd isotopic compositions for the standard in our experiments are $^{87}Sr/^{86}Sr$ = 0.703609 ± 0.000008 (n = 5) and $^{143}Nd/^{144}Nd$ = 0.512978 ± 0.000005 (n = 5), which is consistent with the recommended value [55]. The initial isotopic ratios were calculated from the Rb, Sr, Sm, and Nd concentrations obtained via ICP-MS.

## 4. Results

### *4.1. Zircon U–Pb Ages and Hf Isotopic Compositions*

Zircon grains from the quartz-monzonite sample 87–239 were dated by LA-ICP-MS to obtain the crystallizing age of the North Kudi pluton, and the results are presented in Table S1. Zircon crystals in the sample 87–239 from the North Kudi pluton are pale pink and 150–300 μm in size with length/width ratios of 1.5:1–3:1 (Figure 3). Most zircon grains are characterized by weak or blurred oscillatory magmatic zoning with Th/U ratios ranging from 0.30 to 1.47. Forty-four spot analyses on these zircons yielded a weighted mean $^{206}Pb/^{238}U$ age of 414 ± 2 Ma (2σ, MSWD = 1.6) (Figure 4). Interestingly, there are a few zircon crystals with convoluted textures in CL images (Figure 3). For example, four zircon grains have recrystallized rims with Th/U ratios of 0.36–0.69 (Figure 5), and three zircon crystals have dark cores and bright rims in CL images. Seven spot analyses on these recrystallized areas yielded a weighted mean $^{206}Pb/^{238}U$ age of 373 ± 8 Ma (2σ, MSWD = 1.6) (Figure 4). When all the analysis spots are potted in the coordinate diagram, the Concordia lower intercept age is 403 ± 8 Ma (2σ, MSWD = 3.0).

In situ zircon Lu–Hf isotope analyses were performed on the same area, previously dated by LA-ICP-MS. The results are presented in Table S2 and graphically illustrated in Figure 6. Zircon grains from the North Kudi pluton have $^{176}Hf/^{177}Hf$ of 0.282321–0.282472 with corresponding εHf(t) values of −7.39 to −2.00. The recrystallized areas of zircon grains display a narrow range of $^{176}Hf/^{177}Hf$ from 0.282378 to 0.282450 with εHf(t) from −6.41 to −3.70.

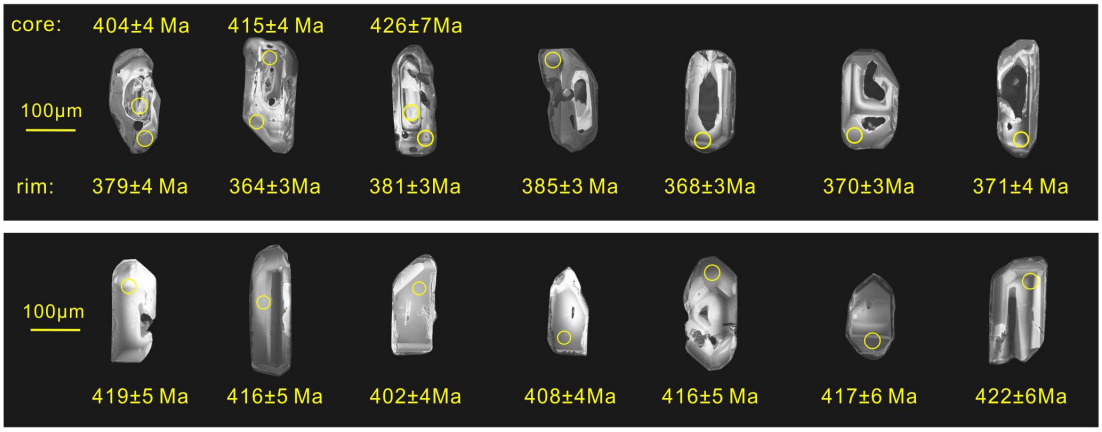


**Figure 3.** Representative cathodoluminescence (CL) images of zircon grains from the North Kudi pluton.

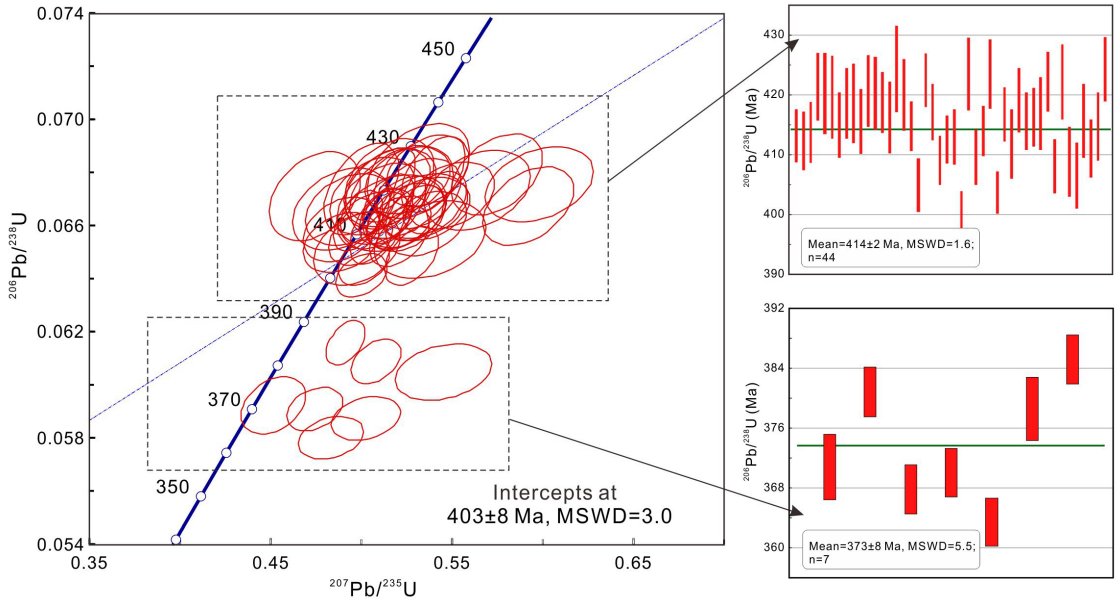


**Figure 4.** Zircon U–Pb Concordia diagrams for the North Kudi pluton.

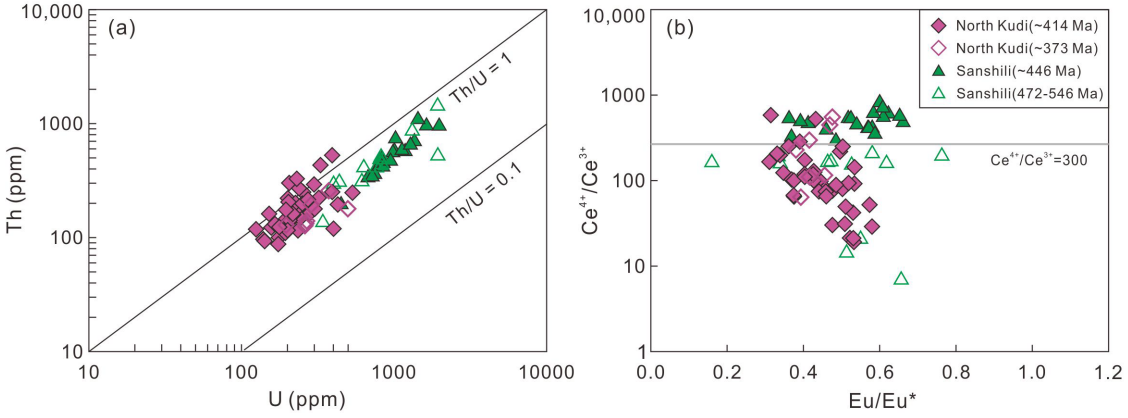


**Figure 5.** Th versus U (**a**) and $Ce^{4+}/Ce^{3+}$ versus Eu/Eu* (**b**) for zircon grains from the North Kudi and the Sanshili pluton in the Western Kunlun orogen. The composition of zircon grains from the Sanshili pluton is from [40].

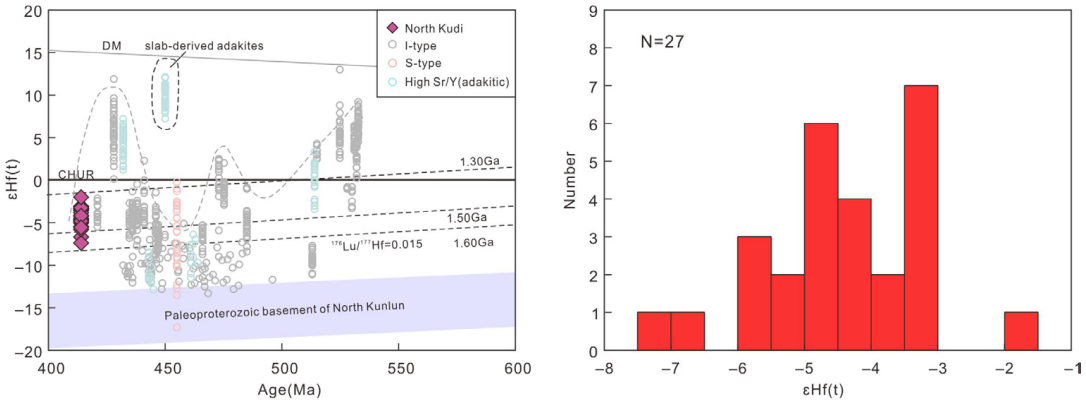


**Figure 6.** Zircon Hf isotopic compositions for samples from the North Pluton. The Hf isotopic compositions of the Early Paleozoic granitoids are from the literature [40].

### *4.2. Whole-Rock Geochemistry*

The present bulk-rock major and trace element data and those from the literature are all given in Table S3. Samples from the North Kudi pluton are mostly plotted in the field of quartz-monzonite, alkali-feldspar granite, and syenogranite (Figure 7a). The quartz-monzonite samples have $SiO_2$ contents of 60.9–65.2 wt.%, MgO contents of 1.09–1.91 wt.%, $Al_2O_3$ contents of 14.7–16.4 wt.% and total alkalis ($Na_2O + K_2O$) contents of 8.22–9.59 wt.%. They are metaluminous and are mostly plotted in the field of quartz-monzonite (Figure 7). These samples are enriched in $K_2O$ (4.44–5.28 wt.%) with affinity to the shoshonitic series (Figure 8). They display LREE-enriched patterns with slightly negative Eu anomalies (Eu/Eu* = 0.72–0.84). In the primitive mantle-normalized diagram, they show enrichment in Rb, Ba, Th, U, Pb, and LREE and depletion in Nb, Ta, Sr, P, and Ti (Figure 9). Notably, all these quartz-monzonite samples have low 10,000 × Ga/Al ratios ranging from 2.16 to 2.97 but high HFSE concentrations (Zr + Nb + Ce + Y = 555–962 ppm).

K-feldspar granite samples have relatively high $SiO_2$ contents of 68.1 wt.% to 71.2 wt.% and $K_2O$ contents of 5.48 wt.% to 6.40 wt.% (Figure 8). The MgO contents of these samples vary from 0.28 wt.% to 0.73 wt.%. Total rare earth element concentrations of these samples range from 345 ppm to 674 ppm, and their REE distribution patterns are also LREE-enriched with $(La/Yb)_N$ of 9–25. However, the negative Eu anomalies (Figure 9) are much stronger than that of the quartz monazite samples. The K-feldspar granite samples are also characterized by high Zr concentrations (339–621 ppm) with 10,000 × Ga/Al ratios of 1.86–3.18. In the primitive mantle-normalized trace element diagram, these samples display a distribution pattern similar to the upper crust. They exhibit positive Th, U, K, and Pb anomalies and negative Ba, Sr, P, and Ti anomalies.

Quart monzonite and K-feldspar granite samples from the North Kudi pluton have low F content from 100 ppm to 240 ppm but high Cl content from 2380 ppm to 2580 ppm. In general, the $P_2O_5$ contents of samples from the North Kudi pluton decrease with increasing $SiO_2$.

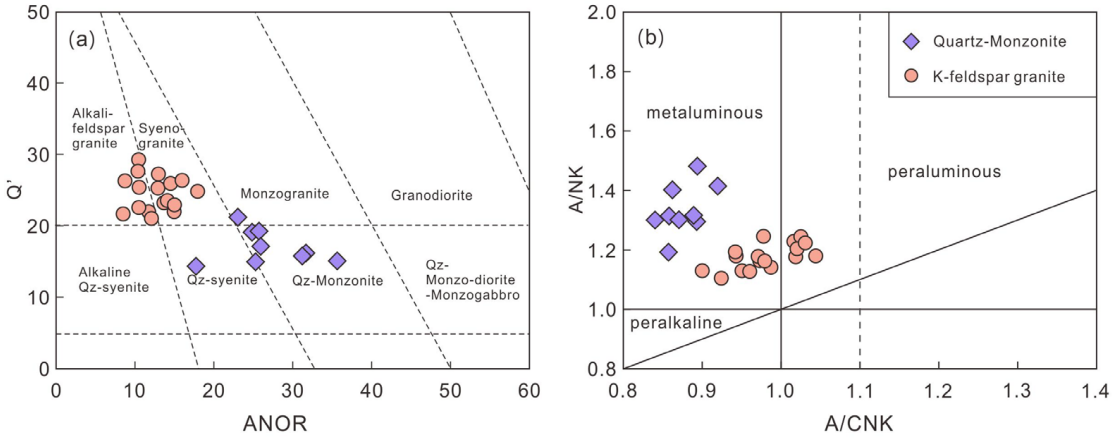


**Figure 7.** Q′-ANOR normative diagram for samples from the North Kudi pluton [56] (**a**,**b**) A/NK versus A/CNK diagram for the North Kudi pluton.

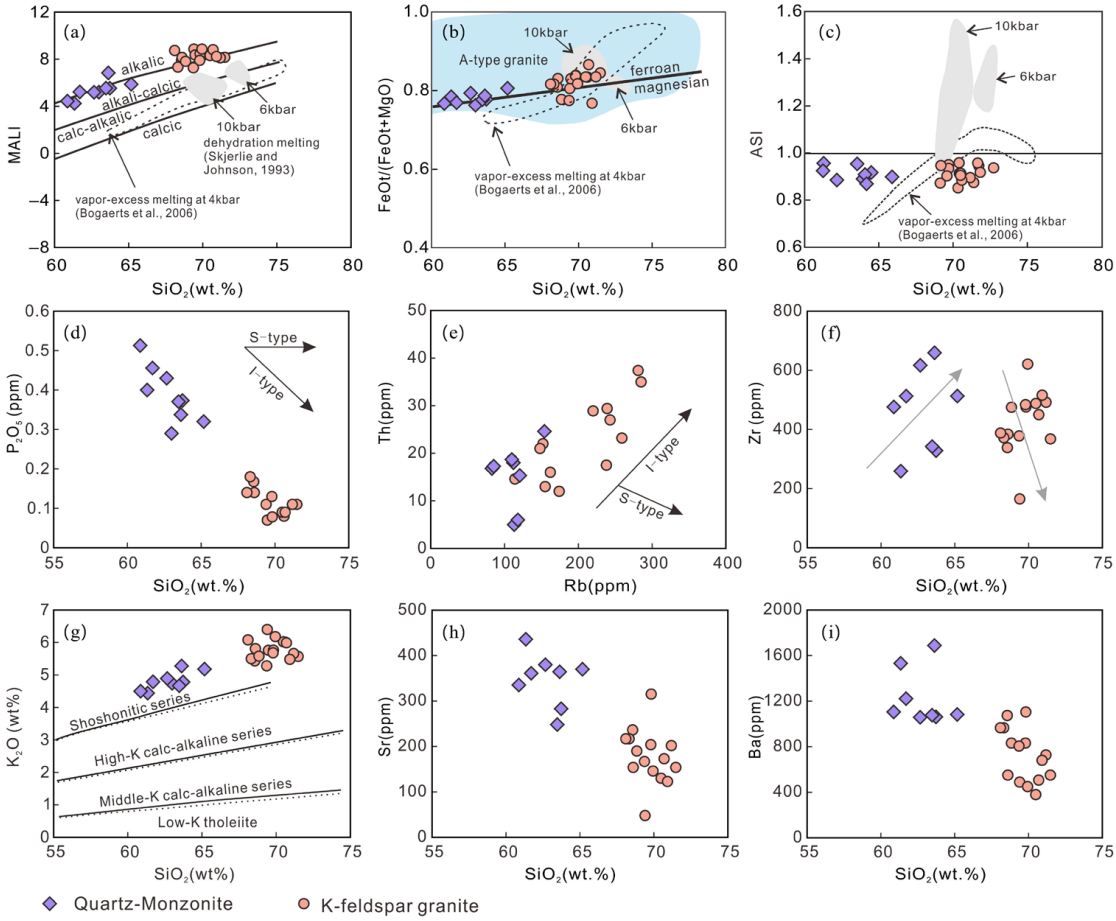


**Figure 8.** Major and trace element compositions of samples from the North Kudi pluton. MALI versus $SiO_2$ (**a**), $FeO^t/(FeO^t + MgO)$ versus $SiO_2$ (**b**), and ASI versus $SiO_2$ (**c**) are after [18]. (**d**–**i**): Harker diagrams for samples from the North Kudi pluton.

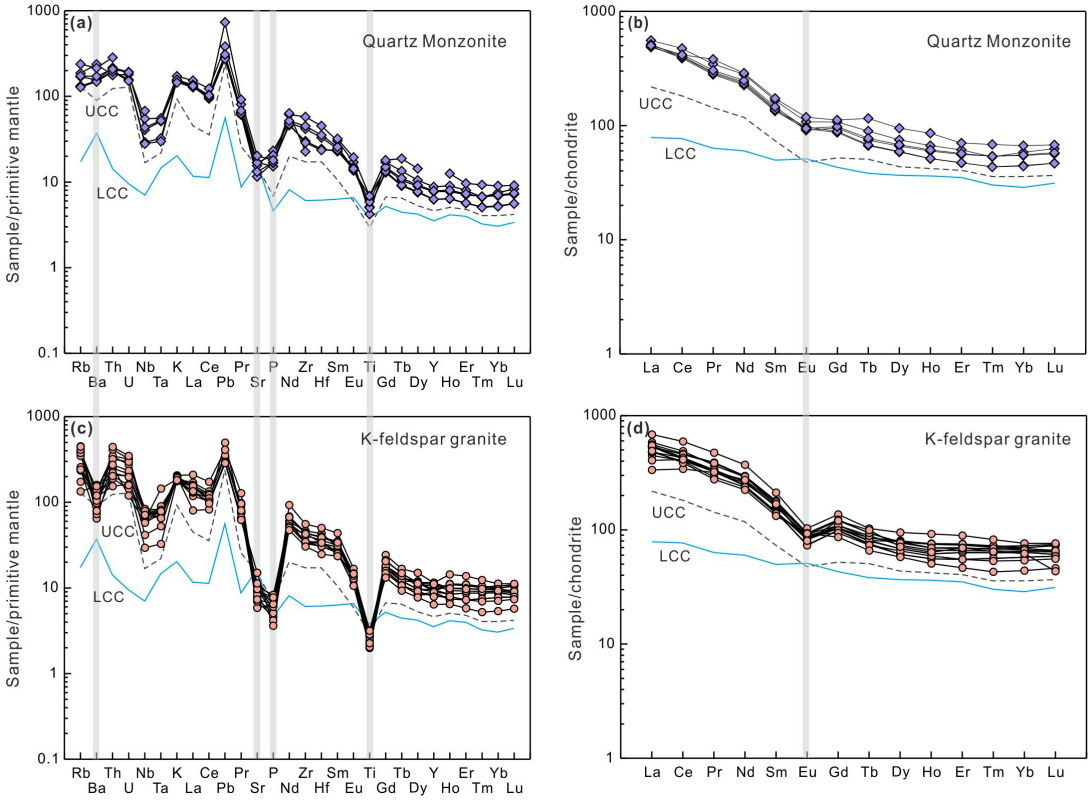


**Figure 9.** Primitive mantle-normalized trace element (**a**,**c**) and chondrite-normalized REE (**b**,**d**) distribution diagrams for quartz-monzonite and K-feldspar granite samples from the North Kudi pluton. LCC = lower continental crust, UCC = upper continental crust. Data used for normalization are from [57].

### *4.3. Sr–Nd Isotopic Compositions*

The Sr–Nd isotopic data are given in Table S3. The present data and those from the literature are all shown in Figure 10. The quartz-monzonite samples from the North Kudi pluton (including literature data) have $(^{87}Sr/^{86}Sr)_i$ of 0.708214 to 0.710415 and εNd(t) of −3.14 to −3.39. K-feldspar granite samples also display a wide variation of $(^{87}Sr/^{86}Sr)_i$ from 0.708244 to 0.710133 but a narrow range of εNd(t) from −4.32 to −2.27 (Figure 10). In summary, samples from the North Kudi have relatively uniform εNd(t) but a variable Sr isotopic composition (Figure 10).

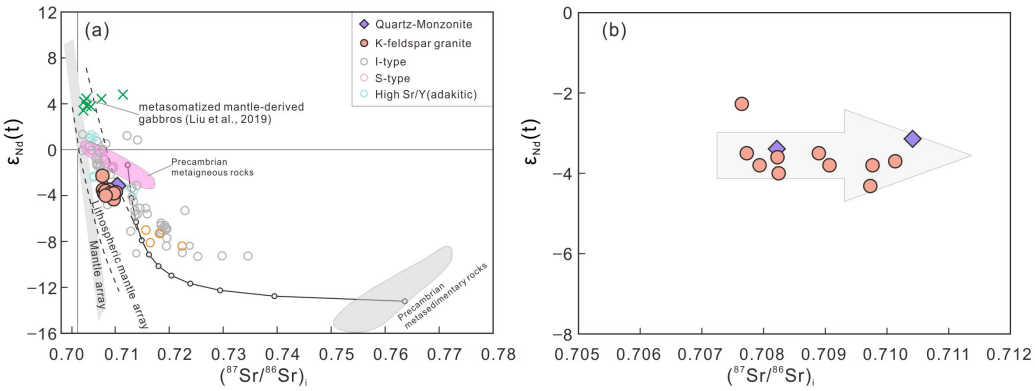


**Figure 10.** Sr–Nd isotopic compositions for samples from the North Kudi pluton. (**b**) is a magnified version of (**a**) to show the nearly constant εNd(t) with increasing $(^{87}Sr/^{86}Sr)i$. Isotopic compositions for Early Paleozoic gabbros and granitoids are all from the literature [40,58]. The field of Precambrian metasedimentary rocks and basaltic rocks in the Kudi ophiolite and MORB are from [26,58].

## 5. Discussion

### *5.1. Geochronology of the North Kudi Granitoids*

Previous geochronological studies on the North Kudi pluton based on Ar–Ar, single zircon TIMS U–Pb, and zircon SHIMP U–Pb methods yielded a wide span of its formation age from ~384 Ma to ~421 Ma [26,27,44]. Zircon is usually crystallized during the early stage of magma evolution and can survive from most late-stage magmatic, metamorphic, and erosional processes [59]. Thus, the zircon U–Pb age can provide the best estimation of the crystallization age for magmatic rocks [40]. However, the single zircon TIMS U–Pb age is unsuitable for zircons with xenocryst cores because the yield age using the single zircon TIMS U–Pb method will be older than the crystallization age of the pluton.

In this paper, we show that some zircon grains contain recrystallized rims. The igneous oscillatory zoning is occasionally visible in the cores (Figure 3). These domains with igneous oscillatory zoning and zircon grains with no core–rim textures yielded a weighted mean age of 414 ± 2 Ma, which is indistinguishable from the SHRIMP zircon U–Pb age of the K-feldspar granite (408 ± 7 Ma) within uncertainties [26,27]. The recrystallized rim yields a mean $^{238}U/^{206}Pb$ age of 373 ± 8 Ma, which is comparable to the biotite $^{40}Ar/^{39}Ar$ age (384.7 ± 5.2 Ma) and also is within the age span of amphibolite facies metamorphism of basic and acidic dykes at the South Kunlun terrane (380–350 Ma) [60,61]. These imply that the crystallization age of the North Kudi pluton is 414 ± 2 Ma. Then, this pluton is likely subjected to a thermal-tectonic event at ~370 Ma when some magmatic zircon grains experienced partial recrystallization. In summary, there is no discernible difference in the crystallization age for the quartz-monzonite and the K-feldspar granite. Therefore, the best estimate for the formation age of the North Kudi pluton is 414 ± 2 Ma.

### *5.2. Geochemical Features of A-Type Granite in the North Kudi Granites*

Aluminous A-type granites with relatively lower $SiO_2$ contents ($SiO_2$ = 65%–72%) in the Lachlan Fold Belt can be distinguished from I-type granites by their high $Na_2O + K_2O$, $FeO^t/(FeO^t + MgO)$, HFSE, REE (with exception of Eu), Ga and Zn, low Ba, Sr, Eu, Cr and Ni concentrations and high magmatic temperature (>900 °C) [5,7,14,62]. K-feldspar granite samples from the North Kudi pluton are characterized by high alkalis ($Na_2O + K_2O$ = 8.22–9.68 wt.%) and high Zr (339–621 ppm) concentration with Zr + Nb + Ce + Y = 555–962 ppm. In the primitive mantle-normalized spider diagram, K-feldspar granite samples from the North Kudi pluton exhibit evident negative Ba, Sr, P, and Ti anomalies. They are plotted into the field of within-plate granites [26,63], and also display high $FeO^t/(FeO^t + MgO)$, and are mostly plotted into the field of ferroan granitoids [18]. In addition, K-feldspar granite is associated with intermediate quartz-monzonite, which also belongs to the shoshonitic series. As shown in Figure 8, the Zr concentration of samples from the North Kudi pluton increases with the increasing $SiO_2$ for quartz-monzonite but is inversely correlated with $SiO_2$ for K-feldspar granite samples. The increasing Zr concentration in quartz-monazite indicates that Zr solubility has not been reached during magma fractionation. Therefore, the minimum estimate of magma temperature is the highest zirconium saturation temperature calculated from the K-feldspar granite samples [64]. In this case, the parent magmas of the North Kudi pluton should be higher than 903 °C. All these features are suggestive of an affinity to A-type granitoids.

According to the classification scheme of [6], K-feldspar granite samples are all plotted in the $A_1$-subgroup granites, which share similar chemical characteristics with oceanic island basalts. Interestingly, the Y/Nb and Ce/Nb of K-feldspar granite and quartz-monazite samples from the North Kudi pluton are positively correlated, with some samples close to the $A_2$-subgroup granitoids. Based on the Dall'Agnol's classification scheme [16,65], these K-feldspar granite samples mostly fall into the field of oxidized A-type granites (Figure 11).

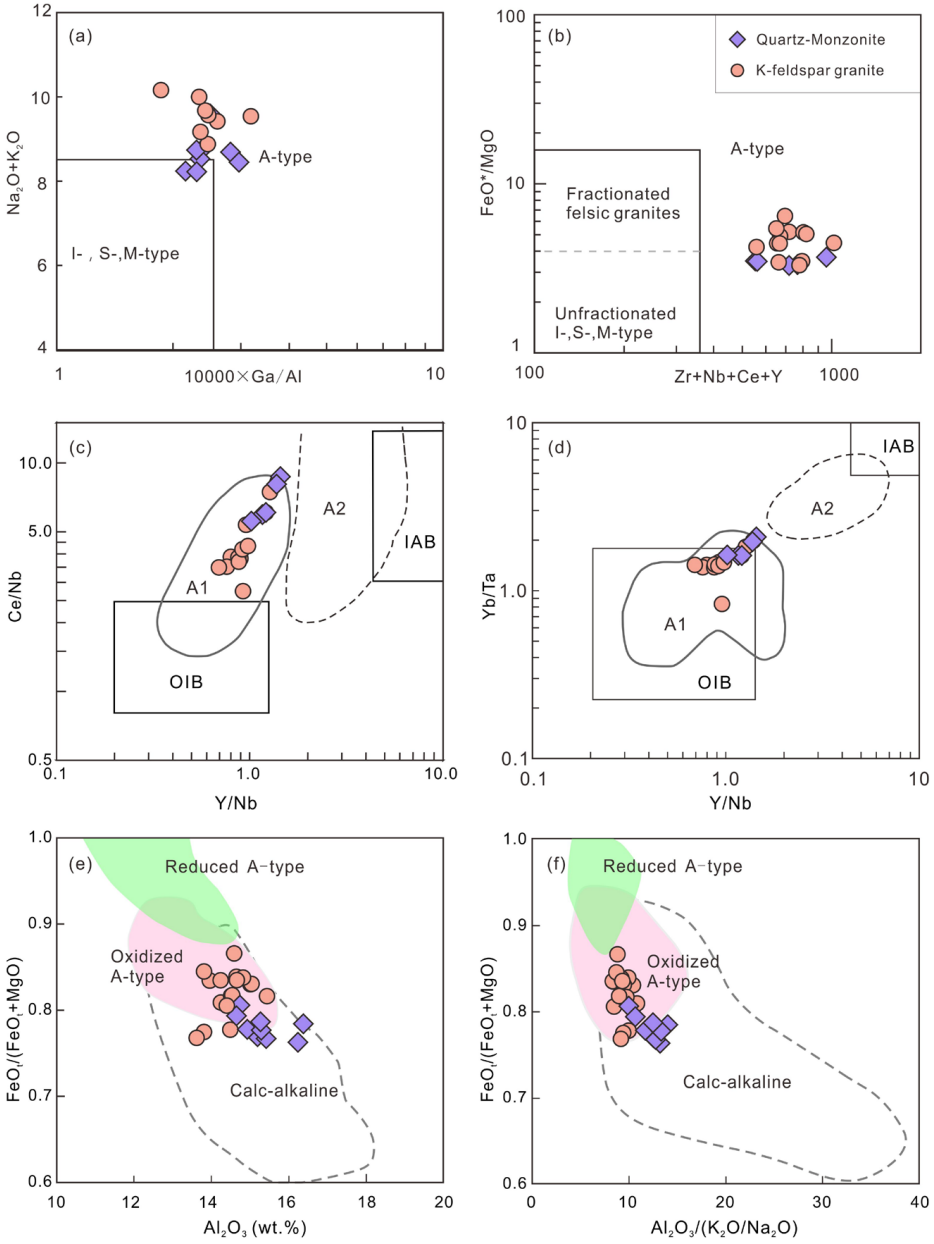


**Figure 11.** Discriminant diagrams to distinguish A granites. $Na_2O + K_2O$ versus 10,000 × Ga/Al (**a**) and FeO*/MgO versus Zr + Nb + Ce + Y (**b**) diagrams [12]; Ce/Nb versus Y/Nb (**c**) and Yb/Ta versus Y/Nb (**d**) diagrams after [6]; $FeO^t/(FeO^t + MgO)$ versus $Al_2O_3$ (**e**) and $FeO^t/(FeO^t + MgO)$ versus $Al_2O_3/(K_2O/Na_2O)$ (**f**) diagrams after [16]. A1-subgroup granite shares similar geochemical characteristics with oceanic-island basalts (OIB), and A2-subgroup granite occur in post-collisional settings with arc-like geochemical compositions.

Even though K-feldspar granite samples from the North Kudi pluton share many geochemical characteristics with the A-type granites, they also exhibit some unique features. Firstly, the most typical characteristic of A-type granites is high Ga/Al (>2.6), but most K-feldspar granite samples are characterized by relatively lower Ga/Al (Figure 11a). On the other hand, the F concentration of samples from the North Kudi pluton is also much lower than Lachlan A-type granites (Figure 12). In addition, unlike aluminous A-type granites in southeastern Australia, which are calc-alkalic and are derived from the partial melting of felsic granulite [5], K-feldspar granite samples from the North Kudi pluton is alkalic to alkali-calcic. Therefore, models for the petrogenesis of the North Kudi pluton

should also address these geochemical characteristics different from the typical A-type granitoids.

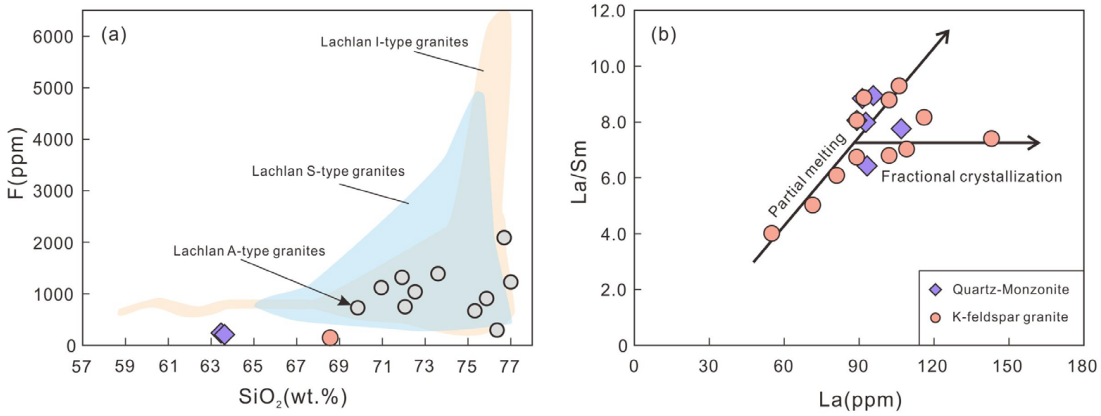


**Figure 12.** F versus $SiO_2$ (**a**) and La/Sm versus La (**b**) for samples from the North Kudi pluton. Data of Lachlan A-type granites and I- and S-type granite fields are from [12].

### *5.3. Petrogenesis of the North Kudi Pluton*

Considering the indistinguishable zircon U–Pb ages, similar Sr–Nd isotopic compositions, and similar mineral assemblages of the K-feldspar granite and the quartz-monzonite, there should be some genetic relationships among different rock types from the North Kudi pluton. It is noted that quartz-monzonite samples from the North Kudi pluton display no discernable negative anomalies of Eu and Ba, and thus cannot be classified as A-type granitoids. Compared with the K-feldspar granite, quartz-monazite has lower $SiO_2$ and higher CaO, Ba, and Sr, which is consistent with relatively low proportions of K-feldspar and high proportions of biotite and plagioclase for quartz-monzonite. As shown in Figure 12, some K-feldspar granite samples deviate from the increasing trend, which indicates that their chemical composition might be partly associated with fractionation crystallization. The decreasing Ba and Sr with increasing $SiO_2$ for samples from the North Kudi pluton indicate fractionation of both plagioclase and K-feldspar (Figure 8). The relatively more robust negative P anomaly of the K-feldspar granite samples and the inversely correlated $SiO_2$ and $P_2O_5$ indicate apatite fractionation. The nearly constant Ta/Nb with decreasing $TiO_2$ suggests the fractionation of magnetite, but there is also a K-feldspar granite sample with relatively high Ta/Nb, which might be associated with the fractionation of biotite (Figure 13). Therefore, the higher $K_2O$ content and occurrence of negative Ba anomaly and more pronounced negative Sr, P, Eu, and Ti anomalies for these K-feldspar granite samples can be attributed to fractionation crystallization (Figure 13).

The magma source is of critical importance in understanding the origin of granite. Since zircon generally crystallizes at the early stage of magma evolution, zircon can hold the original information about the "primitive" magma [40,66]. The low εHf(t) (from −7.39 to −2.00) of zircon grains indicates an enriched magma source, such as sediments, continental crust, or an enriched mantle source [25]. The nearly constant εNd(t) with increasing $(^{87}Sr/^{86}Sr)_i$ for K-feldspar granite and quartz-monzonite samples from the North Kudi pluton precludes the possibility that the North Kudi pluton is derived from the partial melting of the Precambrian metaigneous (amphibolite) and metasedimentary (mica-quartz schist) rocks (Figure 10b) because there are significant differences in εNd(t) for the Precambrian metaigneous and metasedimentary rocks [58]. It is unlikely that the intermediate to felsic magma is derived from a well-mixed source at the lower crust [20,50]. In addition, aluminous A-type granites derived from a lower crustal quartz-feldspathic source are calc-alkalic, and partial melting experiments of quartz-feldspathic crustal rocks at low pressures can only produce high $SiO_2$ melts [18,67–69]. The higher εHf(t) relative to the basement in the Western Kunlun orogen is also against a crustal source of the North Kudi pluton. As shown in Figure 10a, the Sr–Nd isotopic data of samples from the North

Kudi pluton lies along the lithospheric mantle array. There are also several lines of evidence indicating an oxidized metasomatized lithospheric mantle source of the North Kudi pluton. Firstly, the $Ce^{4+}/Ce^{3+}$ ratios of zircon grains from the North Kudi pluton span a wide range from 19 to 583 for ~414 Ma zircon domains (Figure 5). A previous study showed that the ~446 Ma Sanshili pluton contains some old inherited zircon cores from its crustal endmember with lower $Ce^{4+}/Ce^{3+}$, but the involvement of metasomatized mantle wedge-derived magmas makes zircon domains with the age of ~446 Ma with high $Ce^{4+}/Ce^{3+}$ (>300) ratios [40]. Similarly, the existence of high $Ce^{4+}/Ce^{3+}$ (>300) in both ~414 Ma zircon domains indicates that the magma source of the North Kudi pluton contains some oxidized components. Secondly, the chemical compositions of the K-feldspar granite samples are primarily plotted in the field of oxidized A-type granite, which implies a relatively high water content of the magma source of the North Kudi pluton (Figure 11) [16]. Finally, the negative Nb and Ta anomalies of samples from the North Kudi pluton may be inherited from the magma source because the Ta/Nb remains constant with $TiO_2$, which is against the fractionation of Ti-bearing minerals (Figure 13). Combined with the arc-like geochemical characteristics (enriched LILE and depleted HFSE), we suggest that the magma source of the North Kudi pluton seems to be metasomatized by the oxidized $H_2O$-rich components from the subducting slab.

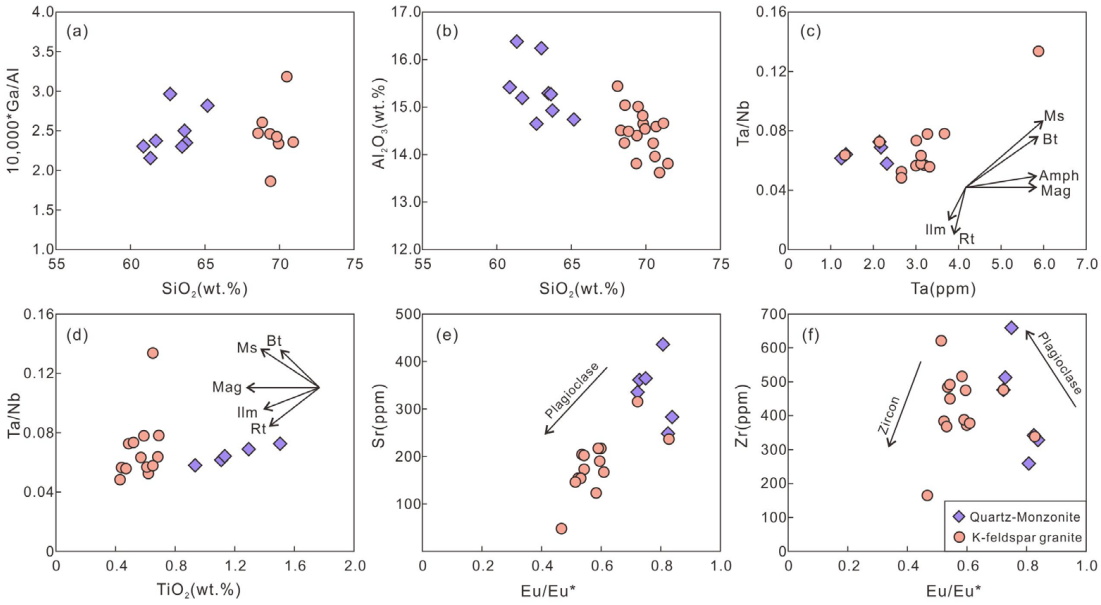


**Figure 13.** Diagrams illustrating the role of fractional crystallization of the North Kudi pluton. (**a**) 10,000 × Ga/Al versus $SiO_2$, (**b**) $Al_2O_3$ versus $SiO_2$, (**c**) Ta/Nb versus Ta, (**d**) Ta/Nb versus $TiO_2$, (**e**) Sr versus Eu/Eu* and (**f**) Zr versus Eu/Eu* diagrams to show the effect of fractional crystallization on the chemical composition variation of samples from the North Kudi pluton.

Samples from the North Kudi pluton have relatively lower F concentration than typical A-type granites in the Lachlan Fold Belt but are enriched in Cl (2380–2580 ppm). The high Cl concentrations in the parental magma of the North Kudi pluton facilitate the fractionation crystallization of plagioclase [5,7,70]. However, the Ga/Al ratio remains unchanged during fractionation (Figure 13), because although plagioclase fractionation can remove Al from the parental magma, Ga can also be removed due to the low abundance of GaF3− 6 complex in the parental magma. This might be partly responsible for the relatively low Ga/Al of the K-feldspar granite samples from the North Kudi pluton.

Fluorite is mainly retained in phengite and apatite during plate subduction, which cannot be released during the early stage of plate subduction [25,71]. In contrast, Cl is hosted in chlorine minerals, which are released at a relatively shallower depth in subduction zones [72–74]. Partial melting of the magma source metasomatized by alkali-rich, high

Cl, and oxidized components would produce the observed geochemical features in the North Kudi pluton. Although samples from the North Kudi pluton are all falling into the field of $A_1$-type granites, the positively correlated Ce/Nb, Yb/Ta, and Yb/Nb can also be accounted for by the involvement of subduction contributions. Combined with the high $K_2O$ and Cl contents, the slab-derived components may contain sediment-derived melts [66,75,76], because the breakdown of phengite will also cause high F concentrations in the metasomatized magma source. On the other hand, considering that their geochemical compositions are similar to $A_1$-type granites, the lithospheric mantle source might be only slightly metasomatized by slab-derived components, or the subduction signatures were diluted by successive injections of asthenosphere-derived melts [77]. The geochemical affinity of K-feldspar granite to A-type granites, especially the negative Ba, Sr, Eu, P, and Ti anomalies, is associated with fractional crystallization.

### *5.4. Geodynamic Implications*

The Early Paleozoic evolution of the Western Kunlun orogen remains controversial due to the lack of HP (high pressure) and UHP (ultra-high pressure) metamorphic rocks. The debates mainly focus on whether the Proto-Tethys exists and whether the Kudi and Qimanyute ophiolite represents the remnants of Proto-Tethys [29,78]. Magmatic rocks can be produced at subduction, syn-collision/accretion, and post-collision/accretion stages of an orogeny, which are of critical importance in understanding magmatic evolution in response to different geodynamic processes [40]. A recent study recognized three episodes of more intensive magmatism at 530–500 Ma, 480–470 Ma, and 445–430 Ma associated with three lithospheric extension events [40]. The last extensional event is related to the closure of the Proto-Tethys at ~442 Ma when slab-derived adakites disappeared in the Western Kunlun orogen, and adakitic rocks were mainly derived from the thickened lower crust. The intermediate-felsic plutons in the Taer region are emplaced at ~432 Ma, which is sourced from the middle and lower crust (30–50 km) with a high melting temperature (876 °C) under an extensional setting [79]. The ~414 Ma North Kudi pluton is formed during the final extensional event in the Western Kunlun orogen and is the latest granitoid intrusion in the Early Paleozoic granite belt. After the closure of the Proto-Tethys, slab break-off or post-collisional delamination cause upwelling of the asthenosphere, which then causes partial melting of a slightly metasomatized lithospheric mantle or a metasomatized lithospheric mantle domain diluted by asthenosphere-derived melts (Figure 14). Fractional crystallization of the metasomatized mantle-derived, alkali-rich, chlorine-rich, and fluorine-poor primary magmas can generate the quartz-monzonite. As a result of continuous magma evolution, K-feldspar granite samples display some typical geochemical features of A-type granites (e.g., negative Ba, Sr, P, and Eu anomalies). Therefore, the intrusion of the North Kudi pluton implies the onset of the post-collisional stage. This conclusion is also supported by the occurrence of subsequent lamprophyre dikes in the Kudi region during the post-collisional extension [61]. In addition, the zircon grains from the North Kudi pluton preserved an age group of 370–380 Ma. The age span is indistinguishable from the Ar–Ar age of the pluton and coincident with the amphibolite facies metamorphic age (380–350 Ma) of basic and acidic dykes in the SKT [28]. This implies that the western part of the Western Kunlun orogen may be subjected to a thermal-tectonic event at ca. 370–380 Ma. Further studies are required to determine the geological significance of such a thermal-tectonic event.

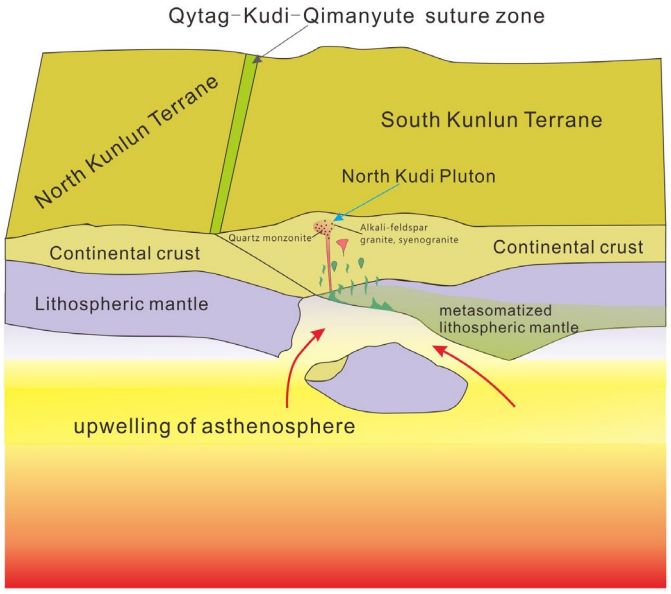


**Figure 14.** Schematic diagram showing the formatting process of the North Kudi pluton. Slab break-off or post-collisional delamination cause upwelling of the asthenosphere [80], which causes partial melting of a slightly metasomatized lithospheric mantle and forms the North Kudi pluton.

## 6. Conclusions

The North Kudi pluton was emplaced at 414 ± 2 Ma, which is likely subjected to a later thermal-tectonic event at ~370 Ma. Samples from the North Kudi pluton are all metaluminous to weakly peraluminous and characterized by high $FeO^t/(FeO^t + MgO)$. K-feldspar granite samples have high $SiO_2$ (68.1–71.2 wt.%), $Na_2O + K_2O$ ($Na_2O + K_2O$ = 8.22–9.68 wt.%), high Zr (339–621 ppm) concentration with Zr + Nb + Ce + Y = 555–962 ppm, and enriched Sr–Nd isotopic compositions with $(^{87}Sr/^{86}Sr)_i$ ranging from 0.708244 to 0.710133 and εNd(t) from −4.3 to −2.27. They also exhibit evident negative Ba, Sr, P, Eu, and Ti anomalies. Their decreasing Zr levels with increasing $SiO_2$ suggests that the temperature of their parent magma should be higher than 903 °C. These features lead the K-feldspar granite to be classified as an A-type granite in the literature. However, K-feldspar granite samples are Cl-rich and F-poor and show relatively low 10,000 × Ga/Al (10,000 × Ga/Al = 1.86–3.18) relative to typical A-type granites.

Quartz-monzonite samples from the North Kudi pluton share similar Sr–Nd isotopic compositions with the K-feldspar granite samples and display relatively lower $SiO_2$ (60.9–65.2 wt.%), total alkalis ($Na_2O + K_2O$) contents (8.22–9.59 wt.%), similar Ga/Al, less pronounced negative Sr, P, and Ti anomalies, and no discernable negative Ba and Eu anomalies. The higher $K_2O$ content and occurrence of negative Ba anomaly and more pronounced negative Sr, P, Eu, and Ti anomalies of the K-feldspar granite samples can be attributed to fractionation crystallization. The nearly constant Ga/Al with magma evolving is caused by the low F concentration because Ga cannot be significantly fractionated from Al during plagioclase fractionation in F-poor magmas. The enriched isotopic compositions, arc-like geochemical features, the involvement of oxidized compositions as indicated by high zircon $Ce^{4+}/Ce^{3+}$ (up to 503), geochemical affinity to oxidized A-type granites, and high Cl and alkali contents suggest that these granitoids were possibly derived from a slightly metasomatized lithospheric mantle or a metasomatized lithospheric mantle domain diluted by melts derived from the upwelled asthenosphere. The emplacement of the North Kudi pluton thus indicates the onset of the post-collisional stage in the Western Kunlun orogen.

Our study also shows that partial melting and fractionation crystallization of these metasomatized mantle-derived, alkali-rich, chlorine-rich, and fluorine-poor magmas can generate some typical geochemical characteristics of A-type granites (e.g., negative Ba, Sr, P,

and Eu anomalies) but has little influence on its Ga/Al because Ga cannot be significantly fractionated from Al during plagioclase fractionation in F-poor magmas.

**Supplementary Materials:** The following supporting information can be downloaded at: https://www.mdpi.com/article/10.3390/min13070941/s1, Table S1: Zircon U-Pb isotopic and compositional data obtained by LA-ICP-MS for samples from the North Kudi pluton; Table S2: Lu-Hf isotope compositions of zircons form the North Kudi pluton; Table S3: Major element (wt.%), trace element (ppm), and Sr-Nd isotopic compositions of samples from the North Kudi pluton [26,44].

**Author Contributions:** Conceptualization, K.W.; methodology, H.Y.; software, M.G.; investigation, K.W., M.G. and X.J.; resources, K.W.; data curation, K.W.; writing—original draft preparation, K.W.; writing—review and editing, K.W., M.L. and M.G.; supervision, K.W.; funding acquisition, H.Y. All authors have read and agreed to the published version of the manuscript.

**Funding:** This research was funded by the National Natural Science Foundation of China (Grants 41903009).

**Data Availability Statement:** The original contributions presented in the study are included in the Supplementary Materials.

**Acknowledgments:** We would like to thank three anonymous reviewers for their constructive comments and suggestions on the early version of our manuscript. This study was supported by the National Natural Science Foundation of China (Grants 41903009). We want to thank Ying Liu, Le Zhang, and Xin Li of the Guangzhou Institute of Geochemistry, Chinese Academy of Sciences, for their assistance in experimental work. We also thank Yuquan Zhang of the Guangzhou Institute of Geochemistry, Chinese Academy of Sciences, for providing samples and helpful discussion.

**Conflicts of Interest:** The authors declare no conflict of interest.

## References

1. Bonin, B. A-type granites and related rocks: Evolution of a concept, problems and prospects. *Lithos* **2007**, *97*, 1–29. [CrossRef]
2. Eby, G.N.; Woolley, A.R.; Ross, M. The A-type granitoids; a review of their occurrence and chemical characteristics and speculations on their petrogenesis. *Lithos* **1990**, *26*, 115–134. [CrossRef]
3. Jiang, X.Y.; Ling, M.X.; Wu, K.; Zhang, Z.K.; Sun, W.D.; Sui, Q.L.; Xia, X.P. Insights into the origin of coexisting A1- and A2-type granites: Implications from zircon Hf-O isotopes of the Huayuangong intrusion in the Lower Yangtze River Belt, eastern China. *Lithos* **2018**, *318–319*, 230–243. [CrossRef]
4. Loiselle, M.; Wones, D. Characteristics and origin of anorogenic granites, geological society of America abstracts with programs. *Geol. Soc. Am.* **1979**, *11*, 468.
5. Collins, W.J.; Beams, S.D.; White, A.J.R.; Chappell, B.W. Nature and origin of A-type granites with particular reference to southeastern Australia. *Contrib. Mineral. Petr.* **1982**, *80*, 189–200. [CrossRef]
6. Eby, G.N. Chemical subdivision of the A-type granitoids; petrogenetic and tectonic implications. *Geology* **1992**, *20*, 641–644. [CrossRef]
7. Whalen, J.B.; Currie, K.L.; Chappell, B.W. A-type granites: Geochemical characteristics, discrimination and petrogenesis. *Contrib. Mineral. Petr.* **1987**, *95*, 407–419. [CrossRef]
8. Jiang, X.; Zhang, Z.; Luo, J.; Wei, L.; Jiang, K. Two-stage, U-mineralization of A-type granites from the Huangmeijian complex, eastern China. *Solid Earth Sci.* **2023**, *8*, 12–24. [CrossRef]
9. Ouyang, L.; Huang, W.; Wu, J.; Liao, J.; Zhang, J.; Chen, X.; Liang, H. Identification of the first Caledonian A-type granitoids in the southern Qin-Hang belt of south China: Tectonic link to early Paleozoic extension. *Solid Earth Sci.* **2023**, *8*, 68–85. [CrossRef]
10. Zhang, Y.; Li, P.; Sun, M.; Yuan, C. Late Paleozoic to early Triassic granitoids from the Rudny Altai, Central Asian Orogenic Belt: Petrogenesis and implications for continental crustal evolution. *Solid Earth Sci.* **2020**, *5*, 115–129. [CrossRef]
11. Zhao, Z.; Yang, X.; Zhang, Z.; Duan, Y. Petrogenesis and geodynamic implications of the Cretaceous anorogenic granitoids in east Qingling orogen. *Solid Earth Sci.* **2021**, *6*, 331–353. [CrossRef]
12. King, P.L.; White, A.J.R.; Chappell, B.W.; Allen, C.M. Characterization and Origin of Aluminous A-type Granites from the Lachlan Fold Belt, Southeastern Australia. *J. Petrol.* **1997**, *38*, 371–391. [CrossRef]
13. Jiang, X.Y.; Li, H.; Ding, X.; Wu, K.; Guo, J.; Liu, J.Q.; Sun, W.D. Formation of A-type granites in the Lower Yangtze River Belt: A perspective from apatite geochemistry. *Lithos* **2018**, *304–307*, 125–134. [CrossRef]
14. Jiang, X.Y.; Luo, J.C.; Guo, J.; Wu, K.; Zhang, Z.K.; Sun, W.D.; Xia, X.P. Geochemistry of I- and A-type granites of the Qingyang-Jiuhuashan complex, eastern China: Insights into early cretaceous multistage magmatism. *Lithos* **2018**, *316–317*, 278–294. [CrossRef]
15. Anderson, J.L.; Morrison, J. Ilmenite, magnetite, and peraluminous Mesoproterozoic anorogenic granites of Laurentia and Baltica. *Lithos* **2005**, *80*, 45–60. [CrossRef]

16. Dall'Agnol, R.; de Oliveira, D.C. Oxidized, magnetite-series, rapakivi-type granites of Carajás, Brazil: Implications for classification and petrogenesis of A-type granites. *Lithos* **2007**, *93*, 215–233. [CrossRef]
17. Patiño Douce, A.E. Generation of metaluminous A-type granites by low-pressure melting of calc-alkaline granitoids. *Geology* **1997**, *25*, 743–746. [CrossRef]
18. Frost, C.D.; Frost, B.R. On ferroan (A-type) granitoids: Their compositional variability and modes of origin. *J. Petrol.* **2011**, *52*, 39–53. [CrossRef]
19. Yang, J.H.; Wu, F.Y.; Chung, S.L.; Wilde, S.A.; Chu, M.F. A hybrid origin for the Qianshan A-type granite, northeast China: Geochemical and Sr–Nd–Hf isotopic evidence. *Lithos* **2006**, *89*, 89–106. [CrossRef]
20. Wu, K.; Zhang, L.P.; Jiang, X.Y.; Zhang, Y.Q.; Sun, W.D.; Yuan, H.L. Geochemical Characteristics and SHRIMP Zircon U-Pb Age of the Putaishan Granite Porphyry and Their Geological Implications. *Geotecton. Metallog.* **2020**, *44*, 986–997.
21. Chen, Y.X.; Cui, Y.; Song, S.G.; Wu, K.; Sun, W.D.; Xiao, T.F. Petrogenesis and tectonic implications of Cambrian Nb-enriched I-and aluminous A-type granites in the North Qilian suture zone. *Int. Geol. Rev.* **2021**, *63*, 1090–1109. [CrossRef]
22. Guo, J.; Zheng, Y.F.; Zhao, Z.F.; Dai, L.Q. Generation of aluminous A-type granite by partial melting of felsic restite: Evidence from Mesozoic granitoids in the southern margin of the North China Craton. *Lithos* **2022**, *428*, 106837. [CrossRef]
23. Gao, Y.J.; Niu, Y.L.; Duan, M.; Xue, Q.Q.; Sun, P.; Chen, S.; Xiao, Y.Y.; Guo, P.Y.; Wang, X.H.; Chen, Y.H. The petrogenesis and tectonic significance of the Early Cretaceous intraplate granites in eastern China: The Laoshan granite as an example. *Lithos* **2019**, *328–329*, 200–211. [CrossRef]
24. Wu, F.Y.; Sun, D.Y.; Li, H.M.; Jahn, B.; Wilde, S. A-type granites in northeastern China; age and geochemical constraints on their petrogenesis. *Chem. Geol.* **2002**, *187*, 143–173. [CrossRef]
25. Li, H.; Ling, M.X.; Ding, X.; Zhang, H.; Li, C.Y.; Liu, D.Y.; Sun, W.D. The geochemical characteristics of Haiyang A-type granite complex in Shandong, eastern China. *Lithos* **2014**, *200*, 142–156. [CrossRef]
26. Liu, Z.; Jiang, Y.H.; Jia, R.Y.; Zhao, P.; Zhou, Q.; Wang, G.C.; Ni, C.Y. Origin of Middle Cambrian and Late Silurian potassic granitoids from the western Kunlun orogen, northwest China: A magmatic response to the Proto-Tethys evolution. *Miner. Petrol.* **2014**, *108*, 91–110. [CrossRef]
27. Xiao, W.J.; Windley, B.; Liu, D.Y.; Jian, P.; Liu, C.Z.; Yuan, C.; Sun, M. Accretionary tectonics of the Western Kunlun Orogen, China: A Paleozoic–Early Mesozoic, long-lived active continental margin with implications for the growth of Southern Eurasia. *J. Geol.* **2005**, *113*, 687–705. [CrossRef]
28. Mattern, F.; Schneider, W. Suturing of the Proto- and Paleo-Tethys oceans in the western Kunlun (Xinjiang, China). *J. Asian Earth Sci.* **2000**, *18*, 637–650. [CrossRef]
29. Wang, J.; Hattori, K.; Liu, J.G.; Song, Y.; Gao, Y.B.; Zhang, H. Shoshonitic- and adakitic magmatism of the Early Paleozoic age in the Western Kunlun orogenic belt, NW China: Implications for the early evolution of the northwestern Tibetan plateau. *Lithos* **2017**, *286–287*, 345–362. [CrossRef]
30. Xiao, W.J.; Han, F.L.; Windley, B.F.; Yuan, C.; Zhou, H.; Li, J.L. Multiple accretionary orogenesis and episodic growth of continents: Insights from the Western Kunlun Range, central Asia. *Int. Geol. Rev.* **2003**, *45*, 303–328. [CrossRef]
31. Li, Y.C.; Xiao, W.J.; Tian, Z.H. Early Palaeozoic accretionary tectonics of West Kunlun Orogen: Insights from Datong granitoids, mafic-ultramafic complexes, and Silurian-Devonian sandstones, Xinjiang, NW China. *Geol. J.* **2018**, *54*, 1505–1517. [CrossRef]
32. Yuan, C.; Sun, M.; Zhou, M.F.; Zhou, H.; Xiao, W.J.; Li, J.L. Absence of Archean basement in the South Kunlun Block: Nd-Sr-O isotopic evidence from granitoids. *Isl. Arc* **2003**, *12*, 13–21. [CrossRef]
33. Wang, C.; Liu, L.; He, S.P.; Yang, W.Q.; Cao, Y.T.; Zhu, X.H.; Li, R.S. Early Paleozoic magmatism in west Kunlun: Constraints from geochemical and zircon U-Pb-Hf isotopic studies of the Bulong granite. *Chin. J. Geol.* **2013**, *48*, 997–1014.
34. Zhu, J.; Li, Q.G.; Chen, X.; Tang, H.S.; Wang, Z.Q.; Chen, Y.J.; Liu, S.W.; Xiao, B.; Chen, J.L. Geochemistry and petrogenesis of the early Palaeozoic appinite-granite complex in the Western Kunlun Orogenic Belt, NW China: Implications for Palaeozoic tectonic evolution. *Geol. Mag.* **2018**, *155*, 1641–1666. [CrossRef]
35. Li, T.F.; Zhang, J.X. Zircon LA-ICP-MS U-Pb ages of websterite and basalt in Kudi ophiolite and the implication, West Kunlun. *Acta Petrol. Sin.* **2014**, *30*, 2393–2401.
36. Han, F.L.; Cui, J.T.; Ji, W.H.; Li, H.P.; Hao, J.W. Discovery of the Qimanyute ophiolite in the West Kunlun and its geological significance. *Geol. Bull. China* **2002**, *21*, 575–578.
37. Cui, J.T.; Wang, J.C.; Bian, X.W.; Luo, Q.Z.; Zhu, H.P.; Wang, M.C.; Chen, G.C. Zircon SHRIMP U-Pb dating of the Dongbake gneissic tonalite in northern Kangxiwar, West Kunlun. *Geol. Bull. China* **2007**, *26*, 726–729.
38. Cui, J.T.; Wang, J.C.; Bian, X.W.; Zhu, H.P. Geological characteristics of Early Paleozoic quartz diorite in the vicinity of Kangxiwar, West Kunlun, China and its zircon SHRIMP U-Pb dating. *Geol. Bull. China* **2006**, *25*, 1450–1457.
39. Wang, J.C.; Cui, J.T.; Luo, Q.Z.; Bian, X.W.; Zhu, H.P.; Yang, K.J.; Peng, H.L.; Zhang, H.P.; Wang, F.; Lin, S.Y. The discovery and tectonic significance of a small branch ocean basin in monggubao-pushouyuan, Tethys ocean of northern Kangxiwa, west Kunlun mountains. *Geol. Shaaxi* **2006**, *24*, 41–50.
40. Wu, K.; Zhang, L.P.; Jiang, X.Y.; Chen, Y.X.; Guo, J.; Sun, W.D.; Sui, Q.L.; Yuan, H.L. Continental crust growth during the evolution of accretionary orogens: Insights from the early Paleozoic granitoids in the Western Kunlun orogen, Northwest China. *Lithos* **2021**, *398–399*, 106253. [CrossRef]
41. Li, B.Q.; Ji, W.H.; Bian, X.W.; Wang, F.; Li, W. The Composition and Geological Significance of the Mazha Tectonic Melange in West Kunlun Mountains. *Geoscience* **2007**, *21*, 78–86.

42. Qu, J.F.; Zhang, L.F.; Ai, Y.L.; Lü, Z.; Wang, J.P.; Zhou, H.; Wang, S.Y. High-pressure granulite from Western Kunlun, northwestern China: Its metamorphic evolution, zircon SHRIMP U-Pb ages and tectonic implication. *Sci. China Ser. D Earth Sci.* **2007**, *50*, 429–441. [CrossRef]
43. Yang, W.Q.; Liu, L.; Cao, Y.T.; Wang, C.; He, S.P.; Li, R.S.; Zhu, X.H. Geochronological evidence of Indosinian (high-pressure) metamorphic event and its tectonic significance in Taxkorgan area of the Western Kunlun Mountains, NW China. *Sci. China Earth Sci.* **2010**, *53*, 15. [CrossRef]
44. Yuan, C.; Sun, M.; Zhou, M.F.; Zhou, H.; Xiao, W.J.; Li, J.L. Tectonic evolution of the West Kunlun: Geochronologic and geochemical constraints from Kudi Granitoids. *Int. Geol. Rev.* **2002**, *44*, 653–669. [CrossRef]
45. Zhang, C.L.; Zou, H.B.; Ye, X.T.; Chen, X.Y. Tectonic evolution of the West Kunlun Orogenic Belt along the northern margin of the Tibetan Plateau: Implications for the assembly of the Tarim terrane to Gondwana. *Geosci. Front.* **2019**, *10*, 973–988. [CrossRef]
46. Jiang, Y.H.; Yang, W.Z. High Contents of Th and U in Late Orogenic Granitoids to Track Lithospheric Delamination: Evidence from Granitoids in Western Kunlun Orogenic Belt, China. *Chin. J. Geochem.* **2000**, *19*, 267–272. [CrossRef]
47. Zhu, J.; Liu, Q.G.; Wang, Z.Q.; Tang, H.S.; Chen, X.; Xiao, B. Magmatism and tectonic implications of early Cambrian granitoid plutons in Tianshuihai terrane of the Western Kunlun orogenic belt, Northwest China. *Northwestern Geol.* **2016**, *49*, 1–18.
48. Hu, J.; Wang, H.; Mu, S.L.; Wang, M.; Hou, X.W. Geochemistry and Hf isotopic compositions of Early Paleozoic granites in Nanpingxueshan from the Tianshuihai Terrane, West Kunlun: Crust-Mantle magmatism. *Acta Geol. Sin.* **2017**, *91*, 16.
49. Zhang, H.S.; He, S.P.; Ji, W.H.; Wang, C.; Shi, J.B.; Kang, K.Y.; Zhang, J.; Zhu, D.W.; Tang, H.W.; Li, C.D.; et al. Implications of Late Cambrian granite in Tianshuihai Massif for the evolution of Proto-Tethys Ocean: Evidences from zircon geochronology and geochemistry. *Acta Geol. Sin.* **2016**, *90*, 21.
50. Wu, K.; Ling, M.X.; Hu, Y.B.; Guo, J.; Jiang, X.Y.; Sun, S.J.; Liang, H.Y.; Liu, X.; Sun, W.D. Melt-Fluxed Melting of the Heterogeneously Mixed Lower Arc Crust: A Case Study from the Qinling Orogenic Belt, Central China. *Geochem. Geophys. Geosyst.* **2018**, *19*, 1767–1788. [CrossRef]
51. Li, X.H.; Tang, G.Q.; Gong, B.; Yang, Y.H.; Hou, K.J.; Hu, Z.C.; Li, Q.L.; Liu, Y.; Li, W.X. Qinghu zircon: A working reference for microbeam analysis of U-Pb age and Hf and O isotopes. *Chin. Sci. Bull.* **2013**, *58*, 8. [CrossRef]
52. Liu, Y.S.; Hu, Z.C.; Gao, S.; Günther, D.; Xu, J.; Gao, C.G.; Chen, H.H. In situ analysis of major and trace elements of anhydrous minerals by LA-ICP-MS without applying an internal standard. *Chem. Geol.* **2008**, *257*, 34–43. [CrossRef]
53. Zhang, L.; Ren, Z.Y.; Xia, X.P.; Li, J.; Zhang, Z.F. IsotopeMaker: A Matlab program for isotopic data reduction. *Int. J. Mass Spectrom.* **2015**, *392*, 118–124. [CrossRef]
54. Bouvier, A.; Vervoort, J.D.; Patchett, P.J. The Lu-Hf and Sm-Nd isotopic composition of CHUR: Constraints from unequilibrated chondrites and implications for the bulk composition of terrestrial planets. *Earth Planet. Sc. Lett.* **2008**, *273*, 48–57. [CrossRef]
55. Wei, G.J. Precise measurement of Sr isotopic composition of liquid and solid base using (LP) MC-ICPMS. *Geochimica* **2002**, *31*, 295–299.
56. Streckeisen, A.; Le Maitre, R. A chemical approximation to the modal QAPF classification of the igneous rocks. *Neues Jahrb. Mineral. Abh.* **1979**, *136*, 169–206.
57. Sun, S.S.; McDonough, W.F. Chemical and isotopic systematics of oceanic basalts: Implications for mantle composition and processes. *Geol. Soc. Lond. Spec. Publ.* **1989**, *42*, 313–345. [CrossRef]
58. Jia, R.Y.; Jiang, Y.H.; Liu, Z.; Zhao, P.; Zhou, Q. Petrogenesis and tectonic implications of early Silurian high-K calc-alkaline granites and their potassic microgranular enclaves, western Kunlun orogen, NW Tibetan Plateau. *Int. Geol. Rev.* **2013**, *55*, 958–975. [CrossRef]
59. Corfu, F.; Hanchar, J.M.; Hoskin, P.W.; Kinny, P. Atlas of zircon textures. *Rev. Mineral. Geochem.* **2003**, *53*, 469–500. [CrossRef]
60. Mattern, F.; Schneider, W.; Li, Y.A.; Li, X.D. A traverse through the western Kunlun (Xinjiang, China): Tentative geodynamic implications for the Paleozoic and Mesozoic. *Geol. Rundsch.* **1996**, *85*, 705–722. [CrossRef]
61. Zhou, H.; Li, J.L. Age and geochemical features of lamprophyres in Kuda, western Kunlun. *Acta Petrol. Sin.* **2000**, *16*, 380–384.
62. Chen, Y.X.; Li, H.; Sun, W.D.; Ireland, T.; Tian, X.F.; Hu, Y.B.; Yang, W.B.; Chen, C.; Xu, D.R. Generation of Late Mesozoic Qianlishan A2-type granite in Nanling Range, South China: Implications for Shizhuyuan W-Sn mineralization and tectonic evolution. *Lithos* **2016**, *266–267*, 435–452. [CrossRef]
63. Pearce, J.A.; Harris, N.B.; Tindle, A.G. Trace element discrimination diagrams for the tectonic interpretation of granitic rocks. *J. Petrol.* **1984**, *25*, 956–983. [CrossRef]
64. Watson, E.B.; Harrison, T.M. Zircon saturation revisited: Temperature and composition effects in a variety of crustal magma types. *Earth Planet. Sc. Lett.* **1983**, *64*, 295–304. [CrossRef]
65. Dall'Agnol, R.; Scaillet, B.; Pichavant, M. An experimental study of a lower Proterozoic A-type granite from the Eastern Amazonian Craton, Brazil. *J. Petrol.* **1999**, *40*, 1673–1698. [CrossRef]
66. Chen, Y.X.; Cui, Y.; Zhang, L.P.; Fu, S.M.; Wu, K.; Song, S.G.; Sun, W.D.; Xiao, T.F. Sediment recycling and adakite petrogenesis: Constraints from the late Ordovician tonalite in the North Qilian suture zone. *Chem. Geol.* **2023**, *624*, 121389. [CrossRef]
67. Bogaerts, M.; Scaillet, B.; Auwera, J.V. Phase equilibria of the Lyngdal granodiorite (Norway): Implications for the origin of metaluminous ferroan granitoids. *J. Petrol.* **2006**, *47*, 2405–2431. [CrossRef]
68. Skjerlie, K.P.; Patiño Douce, A.E.; Johnston, A.D. Fluid absent melting of a layered crustal protolith: Implications for the generation of anatectic granites. *Contrib. Mineral. Petr.* **1993**, *114*, 365–378. [CrossRef]

69. Skjerlie, K.P.; Johnston, A.D. Fluid-absent melting behavior of an F-rich tonalitic gneiss at mid-crustal pressures: Implications for the generation of anorogenic granites. *J. Petrol.* **1993**, *34*, 785–815. [CrossRef]
70. Clemens, J.D.; Holloway, J.R.; White, A.J.R. Origin of an A-type granite; experimental constraints. *Am. Mineral.* **1986**, *71*, 317–324.
71. Qian, L.; Wang, Y.; Xie, J.; Sun, W. The Late Mesozoic granodiorite and polymetallic mineralization in southern Anhui Province, China: A perspective from apatite geochemistry. *Solid Earth Sci.* **2019**, *4*, 178–189. [CrossRef]
72. Wu, K.; Yuan, H.L.; Lyn, N.; Zhang, L.P. The behavior of fluid mobile elements during serpentinization and dehydration of serpentinites in subduction zones. *Acta Petrol. Sin.* **2020**, *36*, 141–153.
73. Wu, K.; Ding, X.; Ling, M.X.; Sun, W.D.; Zhang, L.P.; Hu, Y.B.; Huang, R.F. Origins of two types of serpentinites from the Qinling orogenic belt, central China and associated fluid/melt-rock interactions. *Lithos* **2018**, *302–303*, 50–64. [CrossRef]
74. Wu, K.; Zhang, L.P.; Yuan, H.L.; Sun, W.D.; Deng, J.H.; Zartman, R.E.; Guo, J.; Bao, Z.A.; Zong, C.L. Boron, arsenic and antimony recycling in subduction zones: New insights from interactions between forearc serpentinites and $CO_2$-rich fluids at the slab-mantle interface. *Geochim. Cosmochim. Acta* **2021**, *298*, 21–42. [CrossRef]
75. Zhang, L.P.; Deng, J.H.; Sun, S.J.; Sui, Q.L.; Wang, K.; Sun, W.D. Subduction of the Neo-Tethys ridge beneath the Eurasian continent during the Cretaceous. *Ore Geol. Rev.* **2023**, *154*, 105302. [CrossRef]
76. Zhang, L.P.; Cao, Z.B.; Zartman, R.E.; Li, C.Y.; Sun, S.J.; Liu, L.J.; Sun, W.D. An emerging plume head interacting with the Hawaiian plume tail. *Innovation* **2023**, *4*, 100404. [CrossRef]
77. Wu, K.; Ling, M.X.; Sun, W.D.; Guo, J.; Zhang, C.C. Major transition of continental basalts in the Early Cretaceous: Implications for the destruction of the North China Craton. *Chem. Geol.* **2017**, *470*, 93–106. [CrossRef]
78. Wang, Z.H. Tectonic evolution of the western Kunlun orogenic belt, western China. *J. Asian Earth Sci.* **2004**, *24*, 153–161.
79. Huang, J.G.; Cui, C.L.; Yang, J.; Zhu, Y.Y. Geochemical characteristics and tectonic significance of the Silurian granite rocks in the Taer region of the Western Kunlun. *Geochimica* **2017**, *46*, 11.
80. Zhang, Q.C.; Liu, Y.; Huang, H.; Wu, Z.H.; Zhou, Q. Petrogenesis and tectonic implications of the high-K Alamas calc-alkaline granitoids at the northwestern margin of the Tibetan Plateau: Geochemical and Sr–Nd–Hf–O isotope constraints. *J. Asian Earth Sci.* **2016**, *127*, 137–151. [CrossRef]